

DETC2014-34678

## CONTINUUM ROBOTIC TAIL LOADING ANALYSIS FOR MOBILE ROBOT STABILIZATION AND MANEUVERING

**William S. Rone**

Robotics and Mechatronics Laboratory  
The George Washington University  
Washington, DC, USA

**Pinhas Ben-Tzvi**

Robotics and Mechatronics Laboratory  
The George Washington University  
Washington, DC, USA

### ABSTRACT

*This paper presents the analysis of a continuum robot for use as a robotic tail. The tail is envisioned for use on-board a mobile robot to provide a means separate from the locomotion mechanism (e.g., legs or wheels) to generate external forces and moments to stabilize and/or maneuver the robot. A Cosserat rod model is used to simulate the mechanics of the tail. In these analyses, a prescribed tail configuration (for static analysis) or trajectory (for dynamic analysis) is applied, and the governing equations are used to calculate the loading at the base of the tail, which will be transmitted to the mobile robot. This analysis studies the impact of both trajectory and design factors on the resulting loading profiles. Trajectory factors considered include the mode shape, speed, bending magnitude and bending plane angle. Design factors considered for a fixed mass tail include segment length(s) and mass distribution. This research will ultimately assist future continuum robotic tail designs.*

### NOMENCLATURE

$L$	Total tail length (m)
$L_{1,2}$	Length of tail subsegment 1, 2 (m)
$\mathbf{R}$	Orientation matrix
$\mathbf{f}$	External applied force (N)
$f_{x,y,z}$	x, y, z-component of force at base (N)
$g$	Gravitational acceleration constant (m/s <sup>2</sup> )
$k$	Total segment curvature
$\mathbf{n}$	Internal force (N)
$\mathbf{m}$	Internal moment (N-m)
$\mathbf{n}^{grv}, \mathbf{m}^{grv}$	Internal force, moment due to gravity (N, N-m)
$\mathbf{n}^{inr}, \mathbf{m}^{inr}$	Internal force, moment due to inertia (N, N-m)
$m$	Total tail mass (kg)
$m_{1,2}$	Mass of tail subsegment 1, 2 (kg)
$m_{x,y,z}$	x, y, z component of moment at base (N-m)
$\mathbf{p}$	Global position vector (m)
$r$	Tail core radius (m)

$s$	Distance along the tail (m)
$\mathbf{x}_0$	Global x-direction vector
$\beta$	x-z-plane segment curvature (1/m)
$\gamma$	y-z plane segment curvature (1/m)
$\theta$	Segment bending angle (rad)
$\rho A$	Linear mass density (kg/m)
$\rho \mathbf{J}$	Linear inertia density (kg-m <sup>2</sup> /m)
$\phi$	Bending plane angle (rad)
$\boldsymbol{\omega}$	Global angular velocity (rad/s)
$X_t$	Derivative of X with respect to time
$X_s$	Derivative of X with respect to s
$X^T$	Transpose of X

### INTRODUCTION & BACKGROUND

Bioinspired continuum robotic tails have the capability to enable improved stability and maneuverability in mobile robots by providing a flexible mechanism that generates external force and moment loading on the mobile robot. Examples of tails performing these functions can be found in nature. For example, cheetahs use their tail like a whip to generate dynamic yawing moments for turning in midair when all four running legs are off the ground [1]. Likewise, domesticated cats use their tail as an active counterbalance to stabilize in response to a sudden disturbance while crossing a beam [2]. Other examples also include: a monkey using its tail to help climb, a fish using its tail to generate propulsion, a lizard using its tail to re-orient while jumping, an alligator using its tail for underwater rolling and a kangaroo using its tail as a counterbalance while moving.

Continuum tails will even encourage alternative mobile robot design paradigms. For example, the primary approach for designing bipedal robots has been human-like structures where the torso is carried above the legs, as in Fig. 1(a). However, a continuum tail will enable the robot to carry its torso in front of the legs, with the tail as an active counterbalance behind the

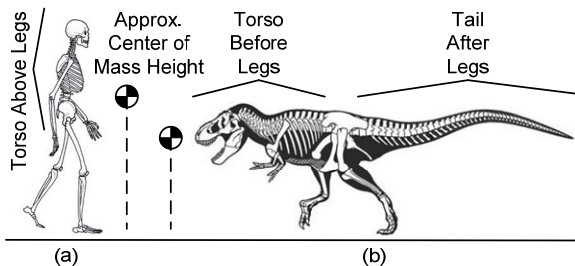


Figure 1. (a) Human-like bipedal locomotion vs. (b) tyrannosaurus-like bipedal locomotion.

legs, similar to a Tyrannosaurus [3], shown in Fig. 1(b). Benefits of this approach include lowering the robot's overall center of mass (COM) for similarly sized robots when standing upright (shown in Fig. 1), and making the legged robot stabilization less like balancing an inverted pendulum and more like balancing a balance scale.

Several mobile robotic systems (particularly legged robots) currently in development could benefit from the inclusion of a continuum tail. For example, the illustrated design concept of the DARPA/Boston Dynamics Cheetah [4] calls for inclusion of a robotic tail to aid in steering. Likewise, the DARPA/Boston Dynamics Atlas [5] has shown the need for a wall to help stabilize the robot as it climbs stairs, using an arm to strike the wall as it climbs. A tail could be used to generate this loading instead, and not require the presence of a wall.

In this paper, a novel continuum tail design inspired by the author's previous continuum robotic systems will be presented. A numerical model for the continuum tail is derived, and a series of numerical case studies on the impact of tail trajectory and design factors on the resulting loading (forces and moments) at the base of the tail are presented. First, however, a summary of previous research in continuum robotics and robotic tails is presented.

## Continuum Robots

Continuum robots differ from conventional robots by exhibiting continuous deformation along the length of the robot instead of finite rotations or translations at discrete joints. Benefits of continuum robots include their inherent compliance, natural whole-arm manipulation and localized actuation. Horn and Anderson [6] presented the first documented research on continuum robots in 1967. However, a renewed focus on this topic in the past 15 years has resulted in a variety of new structures on the meso- and macro-scales for various applications.

On the meso-scale, continuum robots for medical applications, ranging from diagnosis to surgery, have included cable-driven structures [7], rod-driven structures [8] and concentric tube structures [9]. The cable- and rod-driven structures are composed of a solid elastic core along which disks are rigidly mounted. Triplets or quartets of cables or rods are attached to disks along the robot to create different segments, and the mutual loading of these cables or rods determines the robot's shape. The concentric tube robots are

composed of pre-curved flexible tubes nested within one another. By controlling the tubes' relative rotation and translation, the robot's shape can be controlled. Each system's continuum nature allows it to naturally exhibit more gentle interactions with the body when contact occurs compared to conventional surgical tools, while simultaneously preserving the continuum robot's flexibility to navigate within the limited confines of the human body and perform actions such as incising or suturing. However, the continuum tails required in this application will need to be macro-scale structures.

On the macro-scale, previous research has primarily focused on pneumatics-based continuum robots for whole-arm manipulation on-board mobile robots. Two systems developed as part of the DARPA BIODYNOTICS program are the OctArm [10] and the AirOctor [11]. The OctArm utilizes a triplet of McKibben muscle actuations per segment to construct the continuum robot. The relative pressurization of these actuators controls the arm shape. The AirOctor utilizes a pneumatic bellows as the core of the continuum arm with cables routed along the outside of the bellows to control its bending direction and magnitude. The central bellows pressure is regulated to control stiffness. However, in order to develop a continuum tail that can be deployed on mobile robots without a pump (a heavy and vibrating payload), the continuum tail should not require pneumatics.

This research aims to adapt the solid-core cable- and rod-driven continuum robot structures seen in meso-scale applications to the macro-scale. Specifically, the system under consideration will have a solid continuum core, with disks rigidly mounted along its length. A two-segment tail will be considered to study the effectiveness of different tail mode shapes. In addition, a novel hybrid actuation structure will be implemented, with rods actuating segment 1 and cables actuating segment 2.

## Robotic Tails

Previous research into robotic tails has focused primarily on single degree-of-freedom (DOF) planar pendulums included on-board a mobile robots to perform a specific function. TAYLRoACH (Tail Actuated Yaw Locomotion RoACH) [12] utilizes a one-DOF pendulum in the transverse plane to control the robot's yaw angle as it is walking to steer it. Tailbot [13] utilizes a one-DOF pendulum rotating in the sagittal plane to re-orient the pitch of the robot while airborne to match the landing point's ground orientation. Troody [14] utilizes a single DOF pendulum rotating in the sagittal plane to act as an active counterbalance while standing up and walking. Zappa [15] utilizes a single DOF pendulum rotating in the transverse plane to actuate the robot's walking motion.

This research aims to move beyond the paradigm in which the tail only performs a single function for the mobile robot. Generally stated, the tail should be able to generate force in the x-, y- and z-directions, along with moments in the yaw, pitch and roll directions. This will enable the tail to perform actions that can help stabilize the mobile robot in response to multiple

types of external disturbances during locomotion, as well as to help rapidly maneuver the robot.

## SYSTEM DESCRIPTION

A key challenge of this research will be scaling the authors' previously constructed meso-scale continuum robots into the macro-scale structures required for a quadruped or biped robot. Figure 2 shows these two systems used to aid in mechanics model validation for [16],[17]. In each system, linear actuators are used to control the positioning of cable or rods within the mechanism. However, both the length and total mass of the continuum robot will need to be scaled up to generate the required force and moment loading for the legged robots.

Figure 3 shows the design concept for the planned macro-scale continuum tail. The tail will be constructed from a solid elastic core with disks rigidly mounted along its length. A novel two-segment design is planned with the first segment actuated by rods and the second segment actuated by cables (previous continuum robots have utilized only one type of actuation transmission). Rotary servo motors will be used to control the rod and cable positioning. During experimentation, this system will be mounted on a six-axis load cell to measure the force and moment profiles generated by the tail in real-time.

## DYNAMIC TAIL LOADING ANALYSIS

In order to understand how the dynamic tail motion will

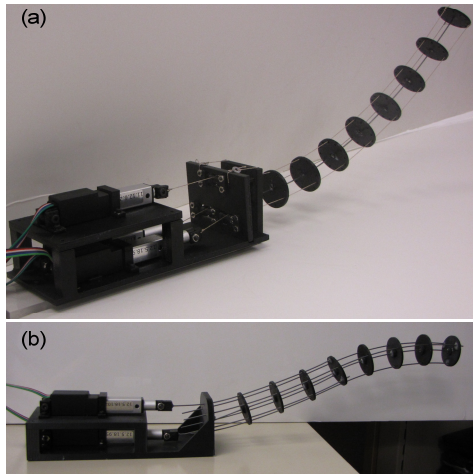


Figure 2. (a) Cable-driven, and (b) rod-driven continuum robots used for model validation.

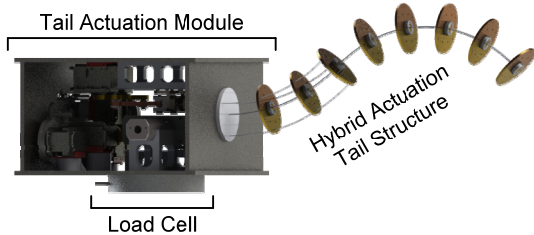


Figure 3. Continuum robotic tail design concept.

load the mobile robot, a Cosserat rod model for the tail inspired by [18] will be used as shown in Eq. (1), where  $s$  is the distance along the tail,  $\mathbf{p}$  is the global position vector,  $\boldsymbol{\omega}$  is the global angular velocity vector,  $\mathbf{R}$  is the orientation matrix,  $\mathbf{n}$  and  $\mathbf{m}$  are the internal force and moment,  $\mathbf{f}$  is the external force,  $\rho A$  is the linear mass density (kg/m) and  $\rho \mathbf{J}$  is the linear moment of inertia density (kg-m<sup>2</sup>/m). Key modeling parameters are illustrated in Fig. 4. Subscripts  $t$  and  $s$  represent derivatives in time and along the tail length, respectively.

$$\begin{aligned} \rho A \mathbf{p}_{tt} &= \mathbf{n}_s + \mathbf{f} \\ (\mathbf{R} \rho \mathbf{J} \mathbf{R}^T \boldsymbol{\omega})_t &= \mathbf{m}_s + \mathbf{p}_s \times \mathbf{n} \end{aligned} \quad (1)$$

Conventionally, these equations of motion are solved by assuming a constitutive model for  $\mathbf{n}$  and  $\mathbf{m}$ , applying the actuation loading as external forces and moments, and solving for the resulting rod positions, velocities, etc. However, in this study, the motion of the rod (or tail) is prescribed, and the resulting force and moment applied at the base of the tail are calculated. Therefore, Eq. (1) can be re-written as Eq. (2). The internal force  $\mathbf{f}$  has been set equal to  $-\rho A g \mathbf{x}_0$  to account for gravitational effects, where  $g$  is the gravitational constant and  $\mathbf{x}_0$  is the global x-direction vector.

$$\begin{aligned} \mathbf{n}_s &= \rho A \mathbf{p}_{tt} + \rho A g \mathbf{x}_0 \\ \mathbf{m}_s &= \mathbf{R} \rho \mathbf{J} \mathbf{R}^T \boldsymbol{\omega}_t + \boldsymbol{\omega} \times \mathbf{R} \rho \mathbf{J} \mathbf{R}^T \boldsymbol{\omega} - \mathbf{p}_s \times \mathbf{n} \end{aligned} \quad (2)$$

These two sets of three scalar equations each are solved using an initial value solver in MATLAB. The boundary condition is set at the tip of the tail ( $s = L$ , Fig. 4), where the internal force and moment are both zero, as shown in Eq. (3). The sets of equations are solved sequentially, first for the  $\mathbf{n}$  values, then the  $\mathbf{m}$  values, due to the dependence of  $\mathbf{m}$  on  $\mathbf{n}$ . In each case, Eq. (2) is integrated from the tip of the tail ( $s = L$ ) to the base ( $s = 0$ ).

$$\mathbf{n}(s=L) = \mathbf{m}(s=L) = \mathbf{0} \quad (3)$$

The baseline parameters of the continuum tail model under consideration are provided in Table 1 for the single- and two-segment structures. Depending on the specific case study, these parameters may be superseded by the range of parameters specified in that case study.

## Trajectory – Continuum Tail Mode Shapes

Trajectories associated with different mode shape of single- and two-segment tails have been applied to the equations of motion in Eq. (2). These trajectories transition

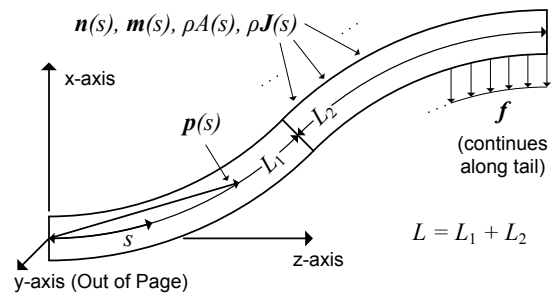


Figure 4. Continuum tail model parameters.

Table 1. Baseline simulation parameters.

Parameter	Single-Segment	Two-Segment
Length (m)	$L = 0.5$	$L_1 = 0.25, L_2 = 0.25$
Tail Radius (m)	$r = 0.01$	$r = 0.01$
Mass (kg)	$m = 2.25$	$m = 2.25$
Mass Distribution	Uniform	Uniform

from an initially straight configuration to one of five maximum deformation configurations shown in Fig. 5, then back to the straight configuration. Table 2 numerically defines the mode shapes, and the trajectories are defined over two 2.5 second spans.

For the trajectories in this paper, sixth-order polynomials are used to generate piecewise continuous and differentiable trajectories over the motion's time spans. In each time span, the curvature velocities and accelerations at the start and end of each time span are all zero. Figure 6 illustrates the tail trajectory of mode M4 from Fig. 5 and Table 2, and includes an inset graph of the segment curvature as a function of time.

Figure 7 shows the x- and z-components of force and the

Table 2. Mode shape trajectories' maximum curvatures.

Mode Shape	S1	M1	M2	M3	M4
Segment 1 $\beta$	$\pi/2L$	$\pi/4L_1$	$\pi/2L_1$	$\pi/4L_1$	$\pi/2L_1$
Segment 2 $\beta$	$\sim$	$\pi/2L_2$	$\pi/4L_2$	$-\pi/2L_2$	$-\pi/4L_2$

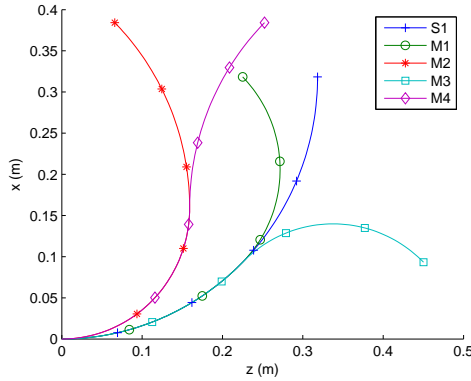


Figure 5. Continuum tail mode shape trajectory maximum deformation for single-segment (S1) and multi-segment (M1-M4) continuum tails.

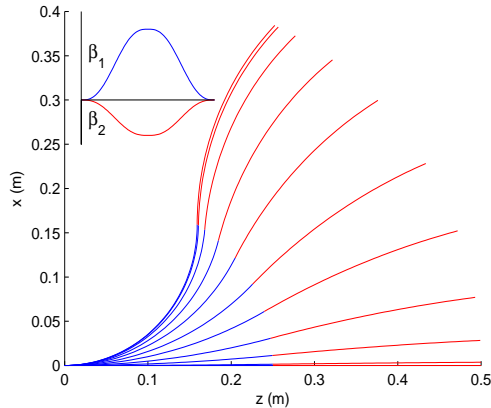


Figure 6. Time-lapse of mode shape M4 tail trajectory with inset plot of segment curvature trajectories

y-component of moment for the five simulations. Because the prescribed motion is in the vertical x-z plane (Fig. 4), all other components are zero. Regardless of the segment curvature magnitude(s) or the relative signs between the two segments, the force and moment loading profiles all have similar shapes. This is because the segment 1 bending controls the overall tail motion, whereas the segment 2 bending is a perturbation of this loading to improve fidelity. Future work will study the effectiveness of other curvature trajectories to quantify the loading profile shapes they can generate.

### Trajectory – Inertial Effects

The shapes of the force and moment graphs in Fig. 7 are dictated by the two effects defining  $\mathbf{n}_s$  in Eq. (2): inertial ( $\rho A \mathbf{p}_t$ ) and gravitational ( $\rho A g \mathbf{x}_0$ ). Because the gravitational effects are time-invariant (they do not depend on velocity or acceleration), they are the same for a prescribed tail path, regardless of the time span over which that path is defined. For example, in Fig. 8(a-c), simulations are run for Case S1 in Fig. 5 with the inertial effects set to zero, using the equations of motion in Eq. (4) to calculate the gravitational loading internal force  $\mathbf{n}^{grv}$  and moment  $\mathbf{m}^{grv}$ , defined over time spans of 3, 4, 5, 6 and 7 seconds. The x-axis is rescaled for each plot to be normalized to the maximum time. As shown, the resulting gravitational loading is identical for all five cases.

$$\begin{aligned} \mathbf{n}_s^{grv} &= \rho A g \mathbf{x}_0 \\ \mathbf{m}_s^{grv} &= -\mathbf{p}_s \times \mathbf{n}^{grv} \end{aligned} \quad (4)$$

However, the inertial effects are time-varying: the greater the acceleration (corresponding in this case to a shorter time span), the greater the inertial effects. Therefore, the acceleration will act as a perturbation to the 'steady-state' gravitational loading profiles. Simulations identical to the above gravitational loading analysis are performed on the equations of motion in Eq. (5) to calculate the inertial loading internal force  $\mathbf{n}^{inv}$  and moment  $\mathbf{m}^{inv}$ . Plots of the non-zero base forces and moment are shown in Fig. 8(d-f). As a secondary verification, it is observed that the sums of the calculated gravitational and inertial effect base loadings ( $\mathbf{n}^{grv}$  and  $\mathbf{n}^{inv}$ ,  $\mathbf{m}^{grv}$  and  $\mathbf{m}^{inv}$ ) equal the total base loading ( $\mathbf{n}$  and  $\mathbf{m}$ , case S1 in Fig. 7).

$$\begin{aligned} \mathbf{n}_s^{inv} &= \rho A \mathbf{p}_t \\ \mathbf{m}_s^{inv} &= \mathbf{R} \rho \mathbf{J} \mathbf{R}^T \boldsymbol{\omega}_t + \boldsymbol{\omega} \times \mathbf{R} \rho \mathbf{J} \mathbf{R}^T \boldsymbol{\omega} - \mathbf{p}_s \times \mathbf{n}^{inv} \end{aligned} \quad (5)$$

It is also noted that the average value of the inertial force or moment in each trajectory time span is zero. This is because the endpoint constraints of each tail trajectory are static configurations of the continuum robot with zero velocity and acceleration. Because there has been no net motion of the tail (i.e., the base frame is fixed at the same location), only deformation, the net inertial force and moment on the body are zero. As a result, a higher accuracy mechanics model of the continuum tail is needed to more accurately represent the inertial effects of the tail. By using a dynamic model of the tail that accounts for the specific actuation mechanism used, with inputs specifying cable or rod displacements, a more realistic

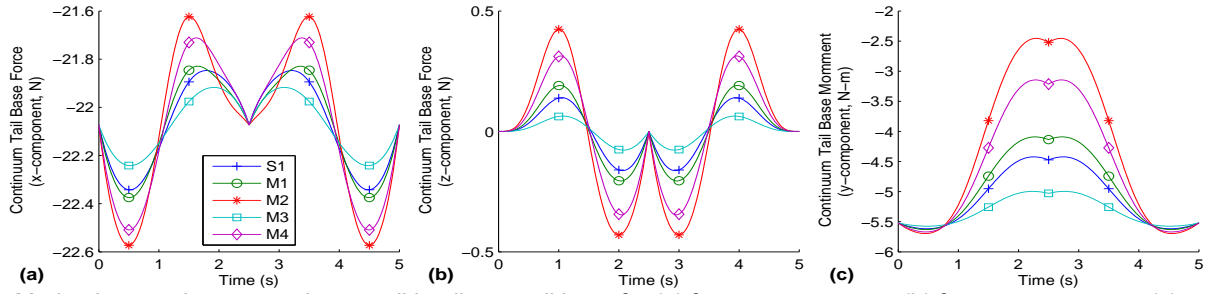


Figure 7. Mode-shape trajectory continuum tail loading at tail base for (a) force x-component, (b) force z-component, (c) moment y-component.

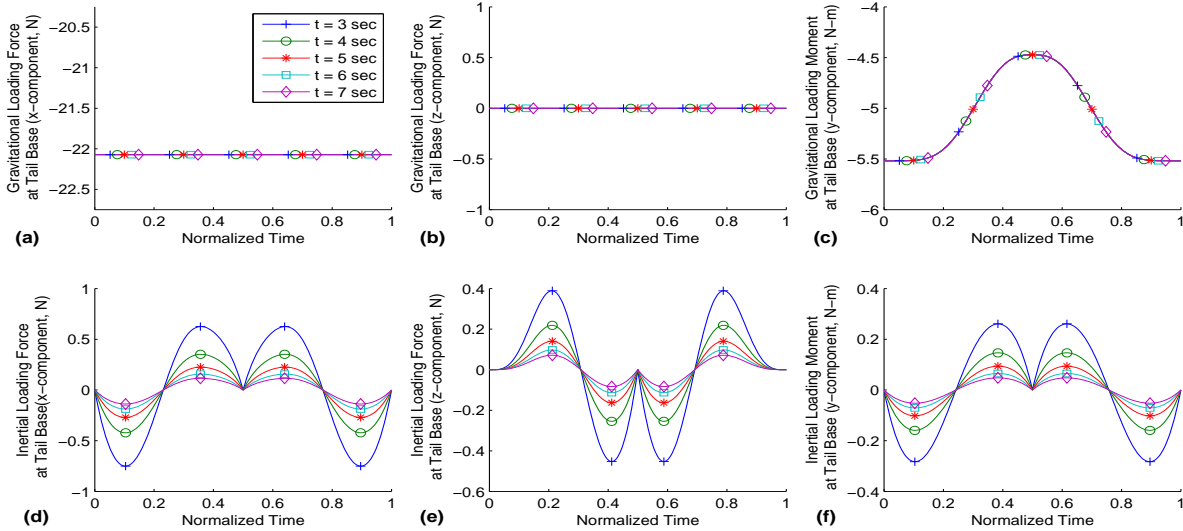


Figure 8. Isolated gravitational (a-c) and inertial (d-f) loading effects for: (a & d) force x-component, (b & e) force z-component, (c & f) moment y-component.

tail trajectory may be generated and analyzed. However, this Cosserat rod approach remains beneficial for understanding the impact of gravitational loading due to its dependence only on the tail's position at a given time, not on the dynamic properties.

### Trajectory – Bending Curvature Magnitude

The single-segment mode-shape case study only considered the tail bending to a prescribed curvature of  $\beta = \pi/2L$ . However, the tail loading will also depend on the bending magnitude. For a fixed tail length  $L$ , the bending angle  $\theta = \beta L$  of the segment will be varied from  $\theta = \pi/6$  rad to  $\theta = \pi$  rad in  $\pi/6$  rad increments. For a fixed time span, the accelerations will be increased as the maximum curvature increases. However, to filter out this effect, only the gravitational effects (Eq. (4)) will be considered. Figure 9 illustrates the y-axis moment (all other force and moment components are time invariant). As expected, the maximum bending moment magnitude decreases as the bending angle increase. This is because the moment arm of the tail's COM decreases as the bending increases from the straight configuration.

This analysis implies that a fully straight configuration may not be ideal as the 'neutral' configuration during

locomotion. If a scenario arose in which the system needed to increase the bending moment magnitude from the starting configuration, it would not be able to do so using gravitational effects if the tail were already fully extended. In addition, any use of inertial effects to increase this magnitude would also need to offset the decrease in moment magnitude due to gravitational effects.

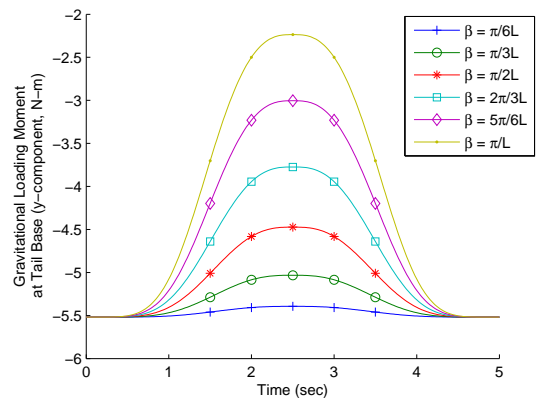


Figure 9. Gravitational effect bending moment profiles for varying maximum curvatures.

## Trajectory – Bending Plane Angle

Thus far, the simulations have held the tail in the vertical x-z plane. However, as the bending plane rotates, some of the loading will re-distribute in different direction and additional loading will be generated. Simulations were run using variations in the bending plane angle  $\phi$  from 0 rad to  $\pi$  rad in  $\pi/6$  rad increments, with a total segment curvature  $k$  of  $\pi/2L$ . The  $\beta$  and  $\gamma$  curvatures are calculated from  $\phi$  and  $k$  using Eq. (6).

$$k^2 = \beta^2 + \gamma^2, \quad \tan \phi = \gamma/\beta \quad (6)$$

Figure 10 illustrates the base loading (forces and moments) for the seven cases specified. Two of the most interesting results are the z-components of the force and moment. The force z-component ( $f_z$ ) is invariant to the bending plane angle because the bending is symmetric around the z-axis. Regardless of the bending plane's rotation, the COM displacement trajectory along the axis remains the same, which directly correlates to the  $f_z$  reaction force that compensates for that COM motion. Likewise, the moment z-component ( $m_z$ ) only depends on the magnitude of the angle between the bending plane and vertical plane, regardless of whether it is above or below the y-z plane. This is because this moment is due to the torsion moment gravity applies to the tail when it bends out of plane. As a result, the greater the out-of-plane bending, the greater the torsional moment. If the bending occurred on the opposite side of the x-z plane, the sign of  $m_z$  would change, applying a negative rolling moment on the mobile robot instead of a positive rolling moment.

The x- and y-components of the force ( $f_x, f_y$ ) and moment ( $m_x, m_y$ ) show the impact of the rotation on the “distribution” of the inertial effects. Over the 0 rad to  $\pi$  rad rotation of the bending plane,  $f_x$  changes sign if the bending plane is above or below the y-z plane, while  $f_y$  does not. This is because the sign of the COM x-coordinate changes from positive to negative during this rotation, whereas the COM y-coordinate is always positive. The opposite would be true if the range of  $\phi$  were  $-\pi/2$

to  $\pi/2$ . Due to the gravitational loading, the x-component forces act around a constant set-point (the tail weight).

The x- and y-components of the moment are complementary to the force components (i.e., zero acceleration x-components force effects correlate to zero acceleration y-component moment effects). However, because the gravitational effects result in a time-varying loading for the y-component of the moment, the moment's inertial effect is superimposed on this trajectory.

## Design – Tail Segment Length(s)

The previous subsections have addressed how trajectory parameters impact the base force and moment loading. However, the tail's design factors will also impact how the tail is able to load the mobile robot. Two design factors will be analyzed in this paper: tail segment length and mass distribution. For the tail segment length analysis, two aspects will be considered for tails with a fixed mass: the impact of total tail length ( $L$ , Fig. 4) for a single-segment tail, and the impact of relative segment lengths ( $L_1$  and  $L_2$ , Fig. 4) in a two-segment tail with fixed total tail length  $L$ .

For the single-segment tail length analysis, the total tail length  $L$  is varied from the value in Table 1. For this analysis, five values of  $L$  from 0.3 m to 0.7 m in 0.1 m increments are compared. For each simulation, the tail moves from zero curvature to  $\pi/2L$  over 2.5 sec, then returns to the fully straight configuration over 2.5 sec. Figure 11(a) illustrates the five continuum tail lengths at their maximum curvature, and Fig. 12(a) illustrates the resulting y-component moment profiles for simulations considering only gravitational effects (Eq. (4)).

As expected, the longer tail provides a greater bending moment due to the longer moment arm of the tail's center of mass. The profiles' magnitudes increase linearly with the length of the tail. However, each moment range as a percentage of the full-extended tail moment (at time zero) remains constant at 18.94%.

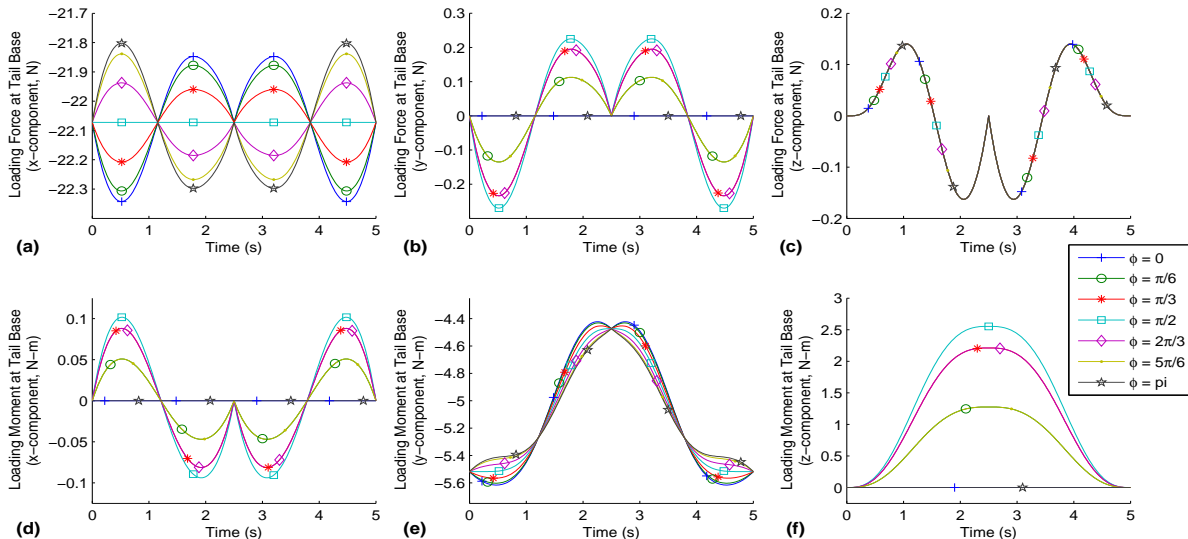


Figure 10. Continuum tail base force: (a) x-component, (b) y-component, (c) z-component, and moment: (d) x-component, (e) y-component, (f) z-component, profiles for bending plane angle analysis.

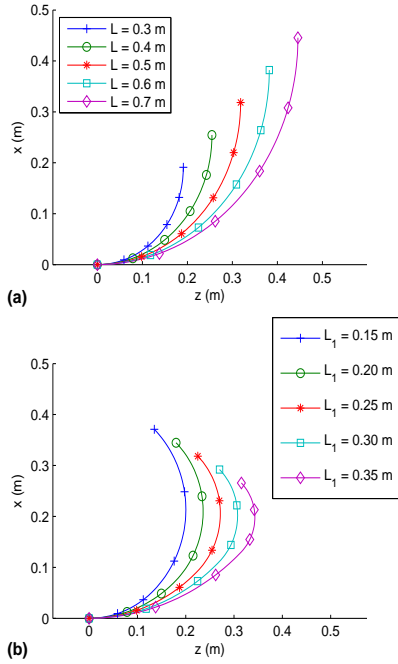


Figure 11. Tail segment length analysis case studies: (a) single-segment total tail length analysis, (b) two-segment relative tail length analysis.

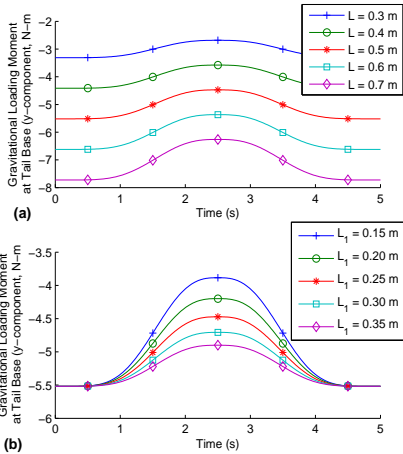


Figure 12. Tail base moment y-component for tail length analysis: (a) single-segment, (b) two-segment.

For the two-segment analysis, the segment 1 length  $L_1$  is varied from the value defined in Table 1. For this analysis, five values of  $L_1$  from 0.15 m to 0.35 m in 0.05 m increments are compared. The second segment length  $L_2$  ensures  $L$  is 0.5 m. Segments 1 and 2 move to maximum curvatures of  $\pi/4L_1$  and  $\pi/2L_2$ , from and to zero curvatures in 2.5 sec time spans. Figure 11(b) illustrates the five cases under consideration at the maximum segment curvatures, and Fig. 12(b) illustrates the resulting moment y-component profile.

Due to the inverse relationship between the first segment curvature and the segment length ( $\beta_1 = \pi/4L_1$ ), a shorter segment will correlate to a greater curvature. Therefore, a greater range of moments can be generated for a prescribed

total tail bending angle by shortening the length of the first segment relative to the second. The lower bound on the length of this segment will be the required strength of the segment to carry the tail's second segment dynamic loading during operation. In addition, if the required segment stiffness is too high (because of its shortened length), the maximum speed will be reduced, which will reduce tail efficacy.

## Design – Mass Distribution

In previous analyses, it was assumed the mass distribution along the tail was uniform. However, the continuum tail may be designed to vary this parameter along the tail. Two aspects of mass distribution will be analyzed: the mass distribution along a single-segment, and the impact of relative mass distribution between two different segments.

For the single-segment analysis, the previously constant linear mass density will be defined as a linear function of the distance along the continuum tail  $s$ . This linear function will be defined by specifying the percentage of maximum linear mass density ( $\rho A_{max}$ ) at the base and tip of the robot, in the format of Base%-to-Tip%. Seven case studies will be compared that change the mass distribution from the uniform density structure previously considered to distributions, including a fully tapered structure. The case studies considered are: 50%-to-100%, 75%-to-100%, 100%-to-100% (uniform), 100%-to-75%, 100%-to-50%, 100%-to-25% and 100%-to-0% (fully-tapered). Two 2.5 sec time spans will define the trajectory, and the tail will be moved from the initially straight configuration to a curvature of  $\pi/2L$ , where  $L$  is 0.5 m, and back to the straight configuration.

Figure 13(a) shows the resulting moment y-component loading at the base due to the gravitational effects (Eq. (4)). As shown, moving a greater proportion of the mass toward the tip increases the moment range for the motion prescribed in this case study. In addition, as the mass distribution becomes more tapered, the greater the impact on the baseline moment.

For the two-segment analysis, the first segment's mass is varied from the previously considered 50% distribution. For this analysis, five mass percentages from 30% to 70% of the tail's total mass in 10% increments are compared, with the second segment mass complementary to ensure the total tail mass is 2.25 kg. When there is a change in density between segments 1 and 2, linear interpolation is used to ensure the density change is continuous across the segment change. This interpolation occurs over a distance  $\pm 0.01$  m surrounding the segment intersection. The trajectory defined for this tail is the same as for the single segments, with maximum curvatures of  $\pi/4L_1$  and  $\pi/2L_2$  for segments 1 and 2, respectively.

Figure 14(b) shows the resulting moment y-component profiles at the base due to the gravitational effects (Eq. (4)). As shown, increasing the second segment mass relative to the first will increase the moment loading by the tail. This distribution also improves the tail's fidelity in controlling the moment: for the 30%-70% distribution, the moment trajectory's range as a percentage of the fully-extended moment is 28.4%, whereas the percentage for the 70%-30% distribution is only 20.1%

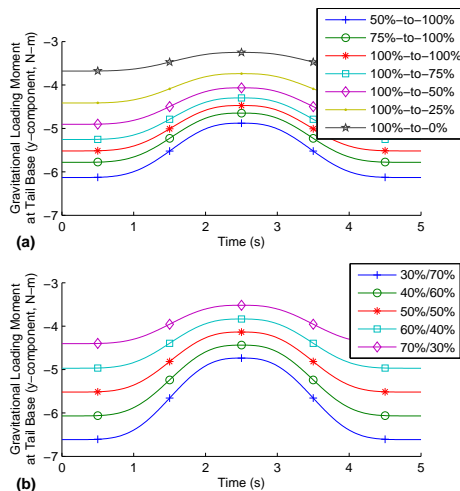


Figure 13. Tail base moment y-component for mass distribution analysis: (a) single-segment, (b) two-segment.

## CONCLUSION

This paper has shown the impact various properties associated with the trajectory and design of a continuum tail have on the resulting loading of that tail at its base. Key conclusions from the analyses include: (a) a non-straight reference configuration for the tail should be used to aid in increasing the moment y-component magnitude during locomotion; (b) a shorter  $L_1$  in a two-segment tail provides greater range of motion of the tail tip for a given segment 1 bending angle and will enable more rapid tail motions due to less required actuation displacement; (c) allocating a larger proportion of the tail's mass in segment 2 and toward the tip provides larger bending moments and greater fidelity of control over the applied moment; and (d) a higher fidelity mechanics model is required for further analysis of the inertial effects.

The analysis presented in this article will be used to help match a continuum tail's design to a given mobile robot's required external loading. As an initial step, this required external loading will be extrapolated from multi-body dynamic simulations of legged locomotion. Case studies will be generated in which both biped and quadruped model will be subjected to external disturbances and required to maneuver without changing their gait. The required loading to counteract these disturbances (stabilizing) or to achieve the desired motion (maneuvering) will be calculated, and the continuum tail will be designed to achieve the maximum required loading with a safety factor. The design factors to be impacted will include the tail's stiffness and actuator strength, which will affect the tail's maximum acceleration, and its mass and mass distribution, which will impact both the tail's inertial and gravitational loading.

## ACKNOWLEDGMENTS

This material is based upon work supported by the National Science Foundation under Grant No. 1334227.

## REFERENCES

- [1] R. Briggs, J. Lee, M. Haberland, S. Kim, "Tails in Biomimetic Design: Analysis, Simulation, and Experiment," IEEE/RSJ Int'l Conf. on Intelligent Robots & Systems, 2012, pp. 1473–1480.
- [2] C. Walker, C. J. Vierck Jr., and L. A. Ritz, "Balance in the Cat: Role of the Tail and Effects of Sacrocaudal Transection," *Behav. Brain Res.*, vol. 91, pp. 41–47, 1998.
- [3] M. J. Benton, "Studying Function and Behavior in the Fossil Record," *PLoS Biol.*, vol. 8, no. 3, Mar. 2010.
- [4] Boston Dynamics, "Cheetah - Fastest Legged Robot," 2012. [Online]. Available: [http://www.bostondynamics.com/robot\\_cheetah.html](http://www.bostondynamics.com/robot_cheetah.html). [Accessed: 12-Feb-2013].
- [5] Boston Dynamics, "Atlas - The Agile Anthropomorphic Robot," 2013. [Online]. Available: [http://www.bostondynamics.com/robot\\_atlas.html](http://www.bostondynamics.com/robot_atlas.html). [Accessed: 25-Nov-2013].
- [6] R. C. Horn and V. C. Anderson, "Tensor Arm Manipulator Design," *ASME Pap.*, p. 67–DE–57, 1967.
- [7] D. B. Camarillo, C. F. Milne, C. R. Carlson, M. R. Zinn, and J. K. Salisbury, "Mechanics Modeling of Tendon-driven Continuum Manipulators," *IEEE Trans. Robot.*, vol. 24, no. 6, pp. 1262–1273, 2008.
- [8] W. Wei, K. Xu, and N. Simaan, "A Compact Two-Armed Slave Manipulator for Minimally Invasive Surgery of the Throat," in *IEEE/RAS-EMBS International Conference on Biomedical Robotics and Biomechanics*, 2006, pp. 769–774.
- [9] P. E. Dupont, J. Lock, B. Itkowitz, and E. Butler, "Design and Control of Concentric-Tube Robots," *IEEE Trans. Robot.*, vol. 26, no. 2, pp. 209–225, Apr. 2010.
- [10] W. McMahan, V. Chitrakaran, M. A. Csencsits, D. M. Dawson, I. D. Walker, B. A. Jones, M. Pritts, D. Dienno, M. Grissom, and C. D. Rahn, "Field Trials and Testing of the OctArm Continuum Manipulator," in *IEEE International Conference on Robotics and Automation*, 2006, pp. 2336–2341.
- [11] W. McMahan, B. A. Jones, and I. D. Walker, "Design and Implementation of a Multi-section Continuum Robot: Air-Octor," in *IEEE/RSJ International Conference on Intelligent Robots and Systems*, 2005, pp. 2578–2585.
- [12] N. J. Kohut, D. W. Haldane, D. Zarrouk, and R. S. Fearing, "Effect of Inertial Tail on Yaw Rate of 45 Gram Legged Robot," *Int. Conf. Climbing Walk. Robot. Support Technol. Mob. Mach.*, pp. 157–164, 2012.
- [13] E. Chang-Siu, T. Libby, M. Tomizuka, and R. J. Full, "A Lizard-inspired Active Tail Enables Rapid Maneuvers and Dynamic Stabilization in a Terrestrial Robot," 2011 IEEE/RSJ Int'l Conf. on Intelligent Robots and Systems, 2011, pp. 1887–1894.
- [14] "One Small Step for Dinosaurs...TROODY the robotic dinosaur walks the walk," 2002. [Online]. Available: <http://web.mit.edu/spotlight/archives/troody.html>.
- [15] F. J. Berenguer and F. M. Monasterio-Huelin, "Zappa, a Quasi-Passive Biped Walking Robot With a Tail: Modeling, Behavior, and Kinematic Estimation Using Accelerometers," *IEEE Trans. Ind. Electron.*, vol. 55, no. 9, pp. 3281–3289, Sep. 2008.
- [16] W. S. Rone and P. Ben-Tzvi, "Continuum Robot Dynamics Utilizing the Principle of Virtual Power," *IEEE Trans. Robot.*, vol. 30, no. 1, pp. 275–287, February 2014.
- [17] W. S. Rone and P. Ben-Tzvi, "Mechanics Modeling of Multi-Segment Rod-Driven Continuum Robots," *ASME J. Mech. Robot.*, In-Press, 2014. DOI: 10.1115/1.4027235
- [18] D. C. Rucker, R. J. Webster III, "Statics and Dynamics of Continuum Robots with General Tendon Routing and External Loading," *IEEE Trans. Robot.*, vol. 27, no. 6, pp. 1033–1044, 2011.